Journal of Materials Chemistry A

RSC Publishing

PAPER

View Article Online
View Journal | View Issue

Cite this: J. Mater. Chem. A, 2013, 1, 7511

A facile fluorine-mediated hydrothermal route to controlled synthesis of rhombus-shaped Co_3O_4 nanorod arrays and their application in gas sensing†

Zhen Wen, Liping Zhu,* Weimin Mei, Yaguang Li, Liang Hu, Luwei Sun, Weitian Wan and Zhizhen Ye

Received 10th March 2013
Accepted 15th April 2013

DOI: 10.1039/c3ta11004d

www.rsc.org/MaterialsA

We have successfully synthesized rhombus-shaped Co_3O_4 nanorod (NR) arrays *via* a facile fluorine-mediated hydrothermal route involving the formation of Co(OH)F as precursor and then thermal conversion to porous Co_3O_4. The hydrothermal temperature was critical to the rhombic shape of the nanostructures. At low temperatures, the Co^{2+} ions interacted with F^- anions to form CoF^+ complexes and then reacted with OH^- to form rhombus-shaped Co(OH)F. Above 100 °C, the disproportionation of formaldehyde from hydrolysis of hexamethylenetetramine (HMT) hindered the formation of Co(OH)F precursor. In this process, CO_3^{2-} anions direct the dissolution–recrystallization process instead of F^- anions due to stronger affinity of CO_3^{2-} to Co^{2+}. During the transformation from the precursor to the oxide, various annealing temperatures affect the gas sensing performance. The synthesized rhombus-shaped Co_3O_4 NR arrays gas sensor annealed at 450 °C showed the highest sensitivity to ethanol because of good contact, porous structure, good crystallinity, high surface-to-volume ratio and open space.

1 Introduction

Cobalt oxide (Co_3O_4) is considered to be one of the most promising functional materials in many technological areas, such as heterogeneous catalysis,[1] supercapacitors,[2] lithium-ion batteries,[3] and gas sensors.[4] With the development of nanoscience and technology, nanoscaled Co_3O_4 materials have attracted considerable attention in past decades due to their peculiar properties and controllable morphology compared with the bulk phase.[5,6] Research in the area of Co_3O_4 on the nanoscale is motivated by the possibility of controlled synthesis of nanostructured materials with unique properties and various applications. The morphological control, including crystal size, external shape, surface structure, crystal orientation, stacking manners, aspect ratios and even crystalline densities, of nanomaterials is of essential importance.[7,8] Therefore, a large number of efforts have been focused on the controlled synthesis of nanostructured Co_3O_4 and many preparative methods have been developed to synthesize nanomaterials with different morphologies and architectures, such as nanoparticles,[9] nanowires,[10] nanoneedles,[11] nanotubes,[12] nanobelts,[13] nanorods,[1] nanocages,[3] nanostars,[14] and nanoarrays,[15] *etc.* On the other hand, Co_3O_4 nanostructures are often obtained by thermal decomposition of the precursors at elevated temperatures. With such a procedure, the morphology of the Co_3O_4 nanomaterials is largely dependent on the structure of the precursors. Therefore, control of uniform shapes of cobalt salts through proper synthetic strategy plays a significant role in obtaining Co_3O_4 with novel morphologies.[16]

Among Co_3O_4 nanomaterials, one-dimensional (1D) Co_3O_4 nanoarrays have been demonstrated to be an optimized architecture for boosting performance, because of their high reaction rate and great miniaturization potential. Moreover, the nanoscale dimension facilitates taking advantage of the characteristic large length-to-diameter and surface-to-volume ratios. Previously, Wu's group reported the high capacity and rate capability of mesoporous Co_3O_4 nanowire arrays as anodes in lithium-ion batteries.[10] Xue *et al.* synthesized free-standing and well-aligned porous Co_3O_4 nanoneedle arrays growing directly on copper foils for ultrafast charging/discharging of lithium-ion battery anodes.[17] Xia *et al.* prepared single-crystalline Co_3O_4 nanowire arrays grown on a nickel foam for high performance supercapacitor application.[18] Nevertheless, reports about 1D Co_3O_4 nanoarrays for gas sensing application are rare. Various Co_3O_4 nanostructures for high performance gas detection were reported, such as concave Co_3O_4 octahedral mesocrystals for formaldehyde and ethanol detection,[6] meso- and macroporous Co_3O_4 nanorods as an effective volatile organic compounds gas sensor,[19] and Co_3O_4 hollow nanospheres towards toluene and

State Key Laboratory of Silicon Materials, Department of Materials Science and Engineering, Cyrus Tang Center for Sensor Materials and Applications, Zhejiang University, Hangzhou, 310007, P. R. China. E-mail: zlp1@zju.edu.cn; Fax: +86-571-87952625; Tel: +86-571-87953139

† Electronic supplementary information (ESI) available. See DOI: 10.1039/c3ta11004d

acetone vapors,[20] *etc.* Recently, our group synthesized the novel rhombus-shaped Co_3O_4 NR arrays *via* a hydrothermal synthesis approach.[21] However, how to fabricate shape-controlled rhombus-shaped Co_3O_4 nanorod arrays with perfect crystal structure, and identify the possible mechanism governing the formation still remained difficult tasks. Meanwhile, it is worthwhile to study the gas-sensing performance of rhombus-shaped Co_3O_4 NR arrays.

In this work, we report the further study of the controlled synthesis of rhombus-shaped Co_3O_4 nanorod arrays and their application in gas sensors. The fabrication process was elaborated by varying the reaction temperature. In the hydrothermal process, the disproportionation of formaldehyde from hydrolysis of hexamethylenetetramine (HMT) hindered the formation of Co(OH)F precursor at above 100 °C. The material characterization and formation mechanism were investigated by X-ray diffraction (XRD), Fourier transform infrared spectroscopy (FTIR), thermogravimetric analyses (TG), scanning electron microscopy (SEM), transmission electron microscopy (TEM), and X-ray photoelectron spectroscopy (XPS). During the transformation from the precursors to the oxides, various annealing temperatures of the precursor have an effect on the gas sensing performance. The rhombus-shaped porous Co_3O_4 NR arrays showed high-performance for ethanol detection due to the unique structure.

2 Experimental

2.1 Synthesis

The synthesis method was greatly simplified from our previous method.[21] All chemicals were of analytical grade and were used as purchased without further purification. The typical experiments were as follows: 4 mmol (1.16 g) of cobalt nitrate ($Co(NO_3)_2 \cdot 6H_2O$), 8 mmol (0.29 g) of ammonium fluoride (NH_4F) and 8 mmol (1.12 g) of hexamethylenetetramine ($C_6H_{12}N_4$, HMT) were dissolved in 40 mL high purity water (18.3 MΩ cm resistivity) under stirring at room temperature. After stirring for 10 min, the homogeneous solution was transferred into a 50 mL Teflon-lined stainless steel autoclave and then a piece of cleaned titanium (Ti) foil (80 mm × 20 mm) or polycrystalline alumina ceramic plate (8 mm × 4 mm, 0.5 mm in thick) which had been plated with Ag–Pd finger regions (five pairs, both the width and distance are 200 μm) as electrodes were immersed in the reaction solution against the inner wall of the autoclave (Fig. S1, ESI†). Herein, Ti foil was chosen as the substrate for characterization and the ceramic plates for gas-sensing measurements. The autoclave was sealed and maintained at 95 °C for 24 h inside an electric oven. After cooling down to room temperature, the substrate was removed, rinsed with distilled water several times in order to remove the free nanoparticles and the residual reactant, and dried at 60 °C under vacuum for 2 h. Finally, the as-prepared pink precursors were converted to Co_3O_4 *via* thermal decomposition after annealing at 350, 450, 550, 650 and 750 °C in air for 4 h with a heating rate of 10 °C per minute, hereinafter designated as S350, S450, S550, S650 and S750, respectively.

2.2 Characterization

The morphologies of both the precursor and annealed products were investigated using field emission scanning electron microscopy (FESEM, Hitachi S-4800) with an accelerating voltage of 5 kV. The crystal phase identification was investigated by an X-ray diffraction (XRD, Bede D1) system with Cu-Kα radiation ($\lambda = 0.15406$ nm) over the 2θ range of 10–80°. Fourier transformed infrared spectroscopy (FTIR, TENSOR27) was characterized with a DTGS detector by making pellets with KBr powder. Thermogravimetric analysis (TGA, SDT Q600) was carried out under air atmosphere at 10 °C min^{-1} in the temperature range 10–900 °C. Further structural analysis of individual NR was carried out using high-resolution transmission electron microscopy (HRTEM, FEI F20) with an accelerating voltage of 200 kV. Specific surface areas were computed from the results of N_2 adsorption–desorption isotherms at 77 K (Micromeritics ASAP 3020) by using Brunauer–Emmet–Teller (BET). X-ray photoelectron spectroscopy (XPS, Thermo ESCALAB 250) measurements were performed with a monochromatic Al-Kα ($h\nu = 1486.6$ eV) X-ray source. The electrical characteristics were measured at room temperature in the dark using a semiconductor parameter analyzer (Agilent E5270B) with the bias voltage range of −10 to 10 V.

2.3 Gas-sensing measurements

The gas-sensing properties of the rhombus-shaped Co_3O_4 NR arrays were performed on an intelligent gas sensing analysis system (CGS-1TP, Beijing Elite Tech Co., Ltd, China). The sensors were laid on the temperature control and pre-heated at different operating temperatures for about 30 min (Fig. S2, ESI†). Two probes were pressed on sensor electrodes by controlling the position adjustment in the analysis system. When the resistance of the sensor was stable, saturated target gas was injected into the test chamber (18 L in volume) by a micro-injector through a rubber plug. The saturated target gas was mixed with air (relative humidity was about 46%) by two fans. The sensor resistance and sensitivity were collected and analyzed by the system in real time. After the sensor resistance reached a new constant value, the test chamber was opened to recover the sensors in air. The sensitivity response (S) was designated as the ratio R_g/R_a, where R_g is the sensor resistance of a mixture of target gas and air while R_a is in air.

3 Results and discussion

The synthesis includes two steps, the low temperature fluorine-mediated hydrothermal route of preparing rhombic Co(OH)F NR arrays and the pyrolysis of Co(OH)F precursor into porous Co_3O_4, without altering the original shape. The phase composition, morphology and structure of the precursor obtained by the hydrothermal method were firstly investigated systematically. Fig. 1(a) shows the XRD pattern of the precursor, which is indexed as Co(OH)F. The pattern shows very sharp peaks, and except for those arising from the titanium substrate, all of the diffraction peaks in this pattern are in good agreement with the standard Joint Committee on Powder Diffraction Standards

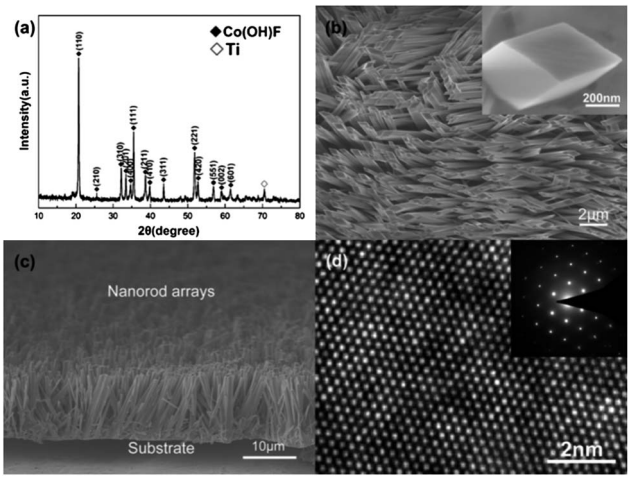

Fig. 1 Phase composition, morphological and structural characterization of the precursor on Ti foil: (a) XRD pattern of the as-prepared Co(OH)F; (b and c) SEM images of Co(OH)F NR arrays; and (d) HRTEM image of a Co(OH)F NR and the corresponding SAED pattern (inset).

(JCPDS) card no. 50-0827, which indicates that the precursor is a pure orthorhombic phase of Co(OH)F and has good crystallinity. From a typical SEM image of the precursor in Fig. 1(b), we can see that large-scale and high density arrays of Co(OH)F NRs uniformly grow on Ti foil. The inset of Fig. 1(b) shows that the NR arrays have a clear-cut rhombic contour with an average edge length of 400 nm and an induced edge angle of around 50°, and the surface of the NRs is smooth. The cross-sectional SEM image shown in Fig. 1(c) indicates that the Co(OH)F NR arrays with a length of about 15 μm are homogeneously well aligned on the Ti foil. The length of the NRs can be controlled by the reaction time in our experiment. The HRTEM and corresponding SAED pattern in Fig. 1(d) and its inset confirm the NRs to be single-crystalline.

Furthermore, we succeeded in producing the rhombus-shaped NR arrays on different supporting substrates (Fig. S3, ESI†), *i.e.*, titanium foil, polycrystalline alumina plate, nickel foil, silicon wafer, glass, *etc.* The method as above can be used to synthesize other materials, which confirms the growth mechanism of rhombus-shaped NRs in our previous report.[21] At the beginning, the Co^{2+} ions interact with F^- ions to form CoF^+ complexes (eqn (1)) and then the OH^- reacts with CoF^+ to form Co(OH)F crystals (according to eqn (2)–(4) below). Functional groups would exist on the surface of the supporting substrates containing chemical defects, hydroxyl and carboxyl or carbonyl groups, which are beneficial to heterogeneous nucleation.[13,21,22] With the assistance of hydrogen bonding, the dangling functional groups act as anchor sites to capture Co(OH)F crystal seeds and make the as-formed crystal seeds stick firmly to the supporting substrate. These crystals agglomerate into rhombic crystalline particles on the surface, and finally form into rhombus-shaped NR arrays. The overall chemical reactions can be expressed with the following formulas:

$$Co^{2+} + F^- \rightarrow CoF^+ \quad (1)$$

$$(CH_2)_6N_4 + 6H_2O \rightarrow 4NH_3 + 6HCHO \quad (2)$$

$$NH_3 + H_2O \rightarrow NH_4^+ + OH^- \quad (3)$$

$$CoF^+ + OH^- \rightarrow Co(OH)F \quad (4)$$

Moreover, the morphologies of the as-prepared precursor are found to be mainly influenced by the growth temperature, which has been discussed in detail as follows. Fig. 2 shows the SEM images of the samples grown on Ti foils at different temperature. At 75 °C, the rhombus-shaped NRs could be clearly observed as shown in Fig. 2(a), sparser than the products prepared at 90 °C as shown in Fig. 2(b). On the temperature rising further, the morphology of rhombic NRs changes dramatically. Fig. 2(c) shows the precursor prepared at 110 °C, where large amounts of nanowires with the diameter ranging from 40 to 60 nm are formed instead of the rhombic nanorods. The nanowires have the trend of bundling into a cluster. When the reaction temperature is 120 °C corresponding to Fig. 2(d), disordered nanowires and nanobelts are obtained. When the temperature is above 130 °C, only extensive nanobelts can be obtained as shown in Fig. 2(e) and (f).

To explain this phenomenon, the chemical composition and phase transition were then investigated intensively. Fig. 3 depicts the XRD and FTIR spectra of precursors at different temperatures, respectively. From the XRD patterns in Fig. 3(a), apparently, typical diffractions of the orthorhombic phase structure of Co(OH)F are observed in the products both prepared at 95 and 110 °C. However, further increasing the growth temperature to 150 °C induces the phase transition, whose diffractions representing $[Co(NH_3)_6]_2(CO_3)_3$ are in accordance with JCPDS card no. 47-0942. The FTIR spectra shown in Fig. 3(b) further confirm the phase transition in detail. In the spectra of the precursor prepared at 95 °C, the strong peaks at ~3574 cm^{-1} and ~1635

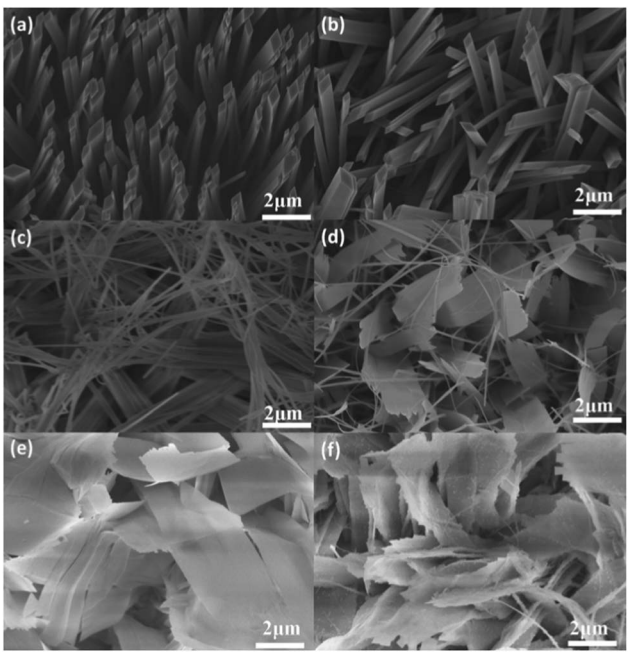

Fig. 2 SEM images of cobalt-precursor nanostructures growing on Ti foil at different hydrothermal temperatures: (a) 75 °C; (b) 95 °C; (c) 110 °C; (d) 120 °C; (e) 130 °C; (f) 150 °C.

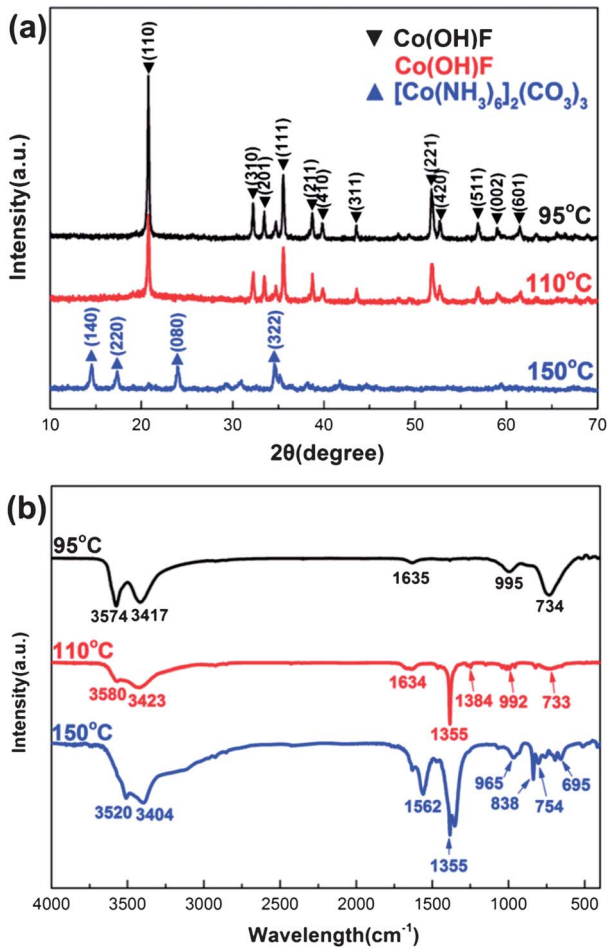

Fig. 3 (a) XRD and (b) FTIR spectra of the precursors obtained at different hydrothermal temperatures.

cm^{-1} are attributed to the stretching vibration of the O–H bond, ν(OH), which is characteristic of molecular water and hydrogen-bonded O–H groups. The shoulder vibration at ~3417 cm^{-1} can be assigned to the O–H groups interacting with fluoride. When the temperature increases to 110 °C, a sharp peak arises at 1355 cm^{-1} corresponding to the symmetric stretching of $\nu_s(COO^-)$, which are the intercalating species in the precursors.[16,23] This indicates that the disproportionation of formaldehyde from hydrolysis of HMT has taken place at this temperature. However, the peaks related to phase transition have not been observed in the XRD pattern in Fig. 3(a) due to the low concentration. It can be observed that the modes at 995 cm^{-1} and 734 cm^{-1} which belong to Co–OH and Co–F, respectively, are completely removed when the temperature reaches 150 °C. The bands at about 965, 838, 754, and 659 cm^{-1} are assigned to the stretching vibrations of ν(C=O), $\delta(CO_3)$, δ(OCO), and ρ(OCO) in the carbonate anion, respectively.[16,24,25] Whereas the asymmetric stretching $\nu_{as}(COO^-)$ (1562 cm^{-1}) and the symmetric stretching $\nu_s(COO^-)$ (1355 cm^{-1}) bands with a wavenumber separation of 207 cm^{-1} confirm the presence of the formate anion in the structure.[16,24] Therefore, a crystal phase transition from the Co(OH)F to the $[Co(NH_3)_6]_2(CO_3)_3$ phase occurs upon increasing temperatures.

In this formation process, the disproportionation of formaldehyde from hydrolysis of HMT is worthy of attention. Since the reaction temperature was low (75 °C), the preferential combination between F^- and Co^{2+} to form CoF^+ complexes prevents the formation of $Co(OH)_2$.[21] With the temperature of the reactant solution increasing to 95 °C, HMT hydrolyzes into formaldehyde and ammonia, acting as a pH buffer to slowly release OH^-. The high concentration of OH^- (due to lower evaporation) react with CoF^+ to form Co(OH)F crystals resulting in rhombus-shaped nanorods with uniform diameters.[26] As the temperature is above 100 °C, the reaction involves disproportionation of the formaldehyde occurring and inducing the carbonate anions which act as a structure directing agent in the dissolution–recrystallization process. Carbonate anions directed the dissolution–recrystallization process instead of fluorine anions.

The affinity to Co^{2+} of different anions is found in the order of $CO_3^{2-} > F^- > OH^-$. The nanowires formed out of bundling of smaller diameter nanowires grow as a bundle individually initially and eventually coalesce to the nanobelts, for which the reason could be lowering of surface energy.[27–29] Consequently, the growth temperature has an obvious impact on the morphology of the precursor, which should be strictly controlled below 100 °C to obtain high aspect ratio nanorod arrays.

The thermodecomposition behaviour of the precursor Co(OH)F was studied by thermogravimetric (TG) analysis. From the TG curve in Fig. 4(a), it is clear to find two apparent decomposition steps. The first step occurs at the temperature below 150 °C and shows a weight loss of 1.10%. The platform of the curve at about 180 °C illustrates the evaporation of adsorbed water. The second step shows an abrupt change of the curve with a weight loss of 15.42% at the temperature above 200 °C corresponding to the theoretical analysis of 15.44% and indicates the oxidation of the precursor.[30] From the known chemical composition of Co(OH)F, the equation of the decomposition reaction in the air can be inferred as the following (eqn (5)):

$$6Co(OH)F + O_2 \rightarrow 2Co_3O_4 + 6HF\uparrow \quad (5)$$

To better understand the possible phase changes, the precursor Co(OH)F is annealed at 350, 450, 550, 650 and 750 °C for 4 h, respectively, to obtain Co_3O_4. Moreover, as the temperature increased from room temperature to 900 °C, weight loss of the sample was less than 17%, which reveals the high thermal stability of Co_3O_4 in air.

The phase structure of the samples after annealing in the air was analyzed by XRD in Fig. 4(b). All of the peaks of the five samples correspond well to the cubic spinel Co_3O_4 phase (JCPDS card no. 43-1003) and no diffraction peaks of Co(OH)F are observed, which reveals the complete thermal conversion of the precursor Co(OH)F to Co_3O_4. The peaks arising from the titanium substrate and titanium dioxide emerged at high temperature and have no influence on our experiments (Fig. S4, ESI†). The mean crystallite sizes are estimated from the (311) peak with the Scherrer formula.[3] The crystallite sizes from S350

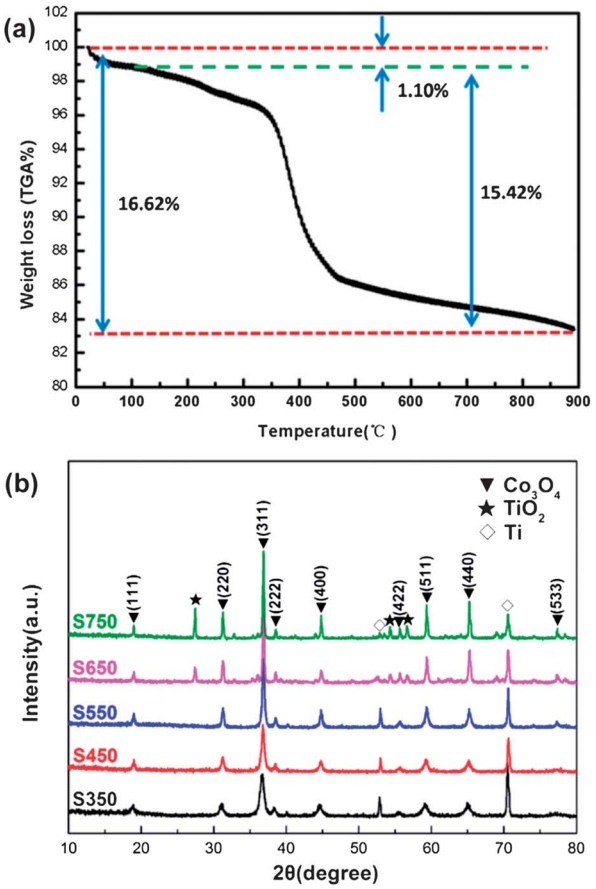

Fig. 4 (a) TG curve under air with a ramp of 10 °C min^{-1} of the precursor Co(OH)F. (b) XRD patterns of rhombus-shaped NR arrays annealed at different temperatures on Ti foil.

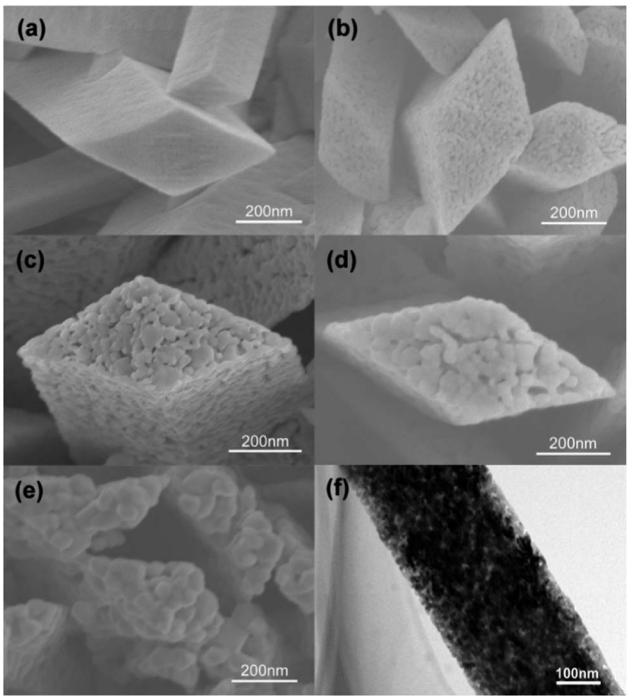

Fig. 5 (a)–(e) SEM images of rhombus-shaped Co_3O_4 NRs annealed at 350 °C, 450 °C, 550 °C, 650 °C and 750 °C, respectively. (f) TEM image of a single NR of the sample annealed at 450 °C.

to S750 are 13.3, 18.1, 24.6, 35.2, and 42.4 nm, respectively (the instrumental error has been deducted). A tendency for minimization of the interfacial surface energy is considered the major factor of crystallite growth during the annealing process.[11,31] The phase changes are also clearly reflected in FTIR spectra (Fig. S5, ESI†), which corresponds with the XRD results.

Fig. 5 shows the high-magnification SEM images of the rhombus-shaped Co_3O_4 NRs obtained at different annealing temperatures and a typical TEM image of a single NR of S450. The SEM image of S350 in Fig. 5(a) shows similar morphology to the precursor and a coarse surface. From Fig. 5(b), it can be observed that pores appeared on the surface of S450, which may be formed due to the dehydration and lattice contraction occurring during the thermal treatment.[11,32] This change leads to the formation of the porous Co_3O_4 rhombus-shaped NRs through the thermal decomposition of the precursor. The S550 can also maintain a basic shape of rhombus-shaped NRs which can be seen from Fig. 5(c), and larger pores occur on the surface. However, the morphology of the S650 has started to change because the rhombus-shaped NRs consist of primary particles that fall into smaller grains, and the initial structures have collapsed, which is displayed in Fig. 5(d), and this change becomes clear for the S750. At 750 °C, the grains gather and recrystallize to a large irregular nanoparticle which can be observed in Fig. 5(e). Ostwald ripening can be used to explain the growth of larger crystals from those of smaller size which have a higher solubility.[3,11,31,32] The typical TEM image of S450 in Fig. 5(f) indicates that a single NR has a diameter of ~400 nm and a porous structure with rough surfaces. The TEM images of other samples are shown in Fig. S6, ESI.† The morphological and size changes are in agreement with SEM observations. From these SEM and TEM images, it can be revealed that different surface morphologies of Co_3O_4 NRs are obtained by thermal decomposition of the precursor Co(OH)F at different temperatures, and the NRs are porous in nature. N_2 sorption was used for gathering information about the specific surface area. The BET surface areas of S350 to S750 were calculated to be 18.7, 12.2, 8.8, 7.6, and 4.8 m^2 g^{-1}, respectively. This difference of BET surface area may impact the gas-sensing property of Co_3O_4 NR arrays.

For further investigation of the chemical composition of the as-prepared Co_3O_4 rhombus-shaped NRs at different annealing temperatures, the XPS measurements were carried out and the spectra is shown in Fig. 6. The binding energies in the XPS analyses were corrected for specimen charging by referring the C 1s peak to 284.8 eV. Fig. 6(a) shows the Co 2p spectra, and the two peaks of each sample are similar, centered at 780.2 and 795.6 eV, corresponding to the Co $2p_{3/2}$ and Co $2p_{1/2}$. The gap between the peaks is about 15 eV (spin–orbit splitting), which also corresponds to the standard Co_3O_4 spectra.[3,33] The major peak of O 1s observed in Fig. 6(b) is 530.1 eV, which can be attributed to the lattice oxygen of Co_3O_4. Besides, a small broadening peak centered at 532.0 eV corresponds to the absorbed species at the surface.[7,33] The F 1s sharp peak in Fig. 6(c) at 684.8 eV can be assigned to the lattice fluorine of

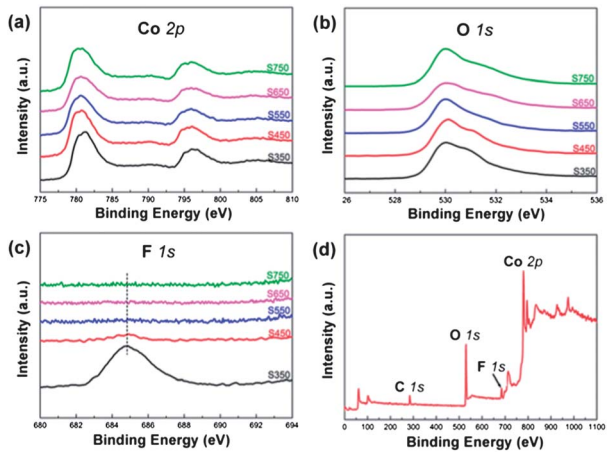

Fig. 6 XPS spectra of the Co_3O_4 NRs: slow scan spectra of (a) Co 2p, (b) O 1s and (c) F 1s; (d) full survey scan spectrum of the sample annealed at 350 °C.

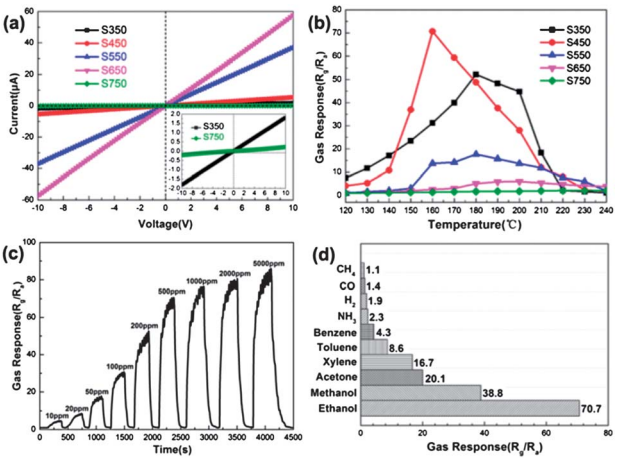

Fig. 7 (a) *I–V* characteristics of five samples between the two neighboring electrodes; (b) gas responses of five samples as a function of different working temperatures to 500 ppm ethanol; (c) the response and recovery curves of S450 between ethanol and air at the operating temperature of 160 °C; (d) the responses of S450 to several reducing gases with concentrations of 500 ppm at 160 °C.

Co(OH)F,[21,34] and the fluorine content of the other samples can be neglected compared to S350. Therefore, S350 was selected to carry out a wide scan between 0 and 1100 eV as is shown in Fig. 6(d), since this sample was achieved at a low temperature and might contain lots of components. The presence of fluorine elements may be related with the incomplete decomposition of Co(OH)F in the heat treatment, which may hinder the electrochemical properties of a p-type semiconductor.

As a result of the large surface areas and porosity revealed in the rhombus-shaped Co_3O_4 NR arrays, they might be advantageous for gas sensing applications. Thus, it is worthwhile to study the gas-sensing performance of Co_3O_4 NR arrays with various surface morphologies. The rhombus-shaped Co_3O_4 NR arrays directly grown on the finger regions are randomly oriented, which provides electrical paths between the fingers. When these Co_3O_4 NRs are randomly oriented, the two electrodes are no longer electrically open. Furthermore, it is noteworthy that the Co(OH)F NRs can still stick to the substrate firmly even after strong ultrasonication over 30 min, suggesting the robust adhesion between the NRs and the supporting substrate. After annealing, such contacts would be much stronger because of the improved crystallinity of the Co_3O_4 NRs. The intensive contact with the substrate would make it possible to use Co_3O_4 NRs directly as gas sensors without the conventional film formation process. Meanwhile, the current–voltage (*I–V*) characteristics of all the samples in Fig. 7(a) show that the current increased linearly with applied bias. Such linear behaviour reveals Ohmic contacts between the nanowires and the electrodes, which is very important for the electrical properties of NRs because this ensures that all upcoming sensing behaviours of sensors represent the properties of the nanorods but not the contact between the nanorods and the electrodes.[19] To make gas sensing measurements, 500 ppm ethanol is introduced into a sealed chamber. As the ethanol is injected, the resistivity of the sample increases exponentially, and recovers to their initial state after exposing them to air, in agreement with that of a typical p-type semiconductor in the entire working temperature range.

The optimal working temperature for maximum sensitivity was determined for each sample and the gas sensing performances of samples S350 to S750 are shown in Fig. 7(b). The responses of all samples were found to increase with the operating temperature, and then decrease with a further rise of the operating temperature. This behavior can be explained by the gas adsorption and desorption kinetics on the surface of Co_3O_4 or similar semiconducting metal oxides.[30,35,36] When the operating temperature is low, the chemical activation of NRs is consequently small, leading to a very small response. When the operating temperature increases, some adsorbed gas molecules may escape before their reaction due to their enhanced activation, thus the response will decrease correspondingly. It is evident that different annealing temperatures lead to a different responses to ethanol vapour. The performance of pure Co_3O_4 for the gas sensors is greatly influenced by its surface area and particle size distribution.[37,38] The sample S450 shows the highest sensitivity and the response to 500 ppm ethanol reaches ~71. The optimal working temperature is about 160 °C, which is much lower than those reported for Co_3O_4 sensors.[37,39,40] As temperature increases, the samples with larger grains and lower specific surface area can be obtained. Therefore, the samples S550–S750 exhibit declining sensitivity. Though it has a larger surface area, the sample S350 shows a slightly worse performance than S450 in the same detection limit. We attribute this behaviour to the residual fluorine element in the Co_3O_4 NRs after calcination at low temperature. Additionally, Co_3O_4 is a p-type semiconductor intrinsically. The density of the holes is of significant importance for the gas-sensing performance.[40,41] Fluorine as a donor impurity will compensate the intrinsic acceptors in Co_3O_4 and thus decrease holes concentration. So the S350 showed an abnormal phenomenon. Therefore, annealing at 450 °C for the rhombus-shaped Co_3O_4 NRs is suggested to be responsible for the optimal ethanol detection.

Finally, a detailed gas-sensing performance of the sample S450 was carried out. Fig. 7(c) shows the typical response and

recovery curves to ethanol with concentrations ranging from 10 to 5000 ppm at the optimal operating temperature of 160 °C. The response increases rapidly with increasing the concentration of ethanol in the range of 10–1000 ppm. Above 1000 ppm, the increase of response turns slow with the ethanol concentration rising. Finally the sensor reaches saturation at about 5000 ppm. The curve shows that the sensor could detect ethanol gas in a wide range of concentrations, starting with the minimum concentration of 10 ppm, which is below the limit (200 ppm) imposed for a breath analyser. Fig. 7(d) shows the responses to several reducing gases at the operating temperature of 160 °C. The gas response to 500 ppm ethanol vapor is 70.7, which is significantly higher than all the other gases under the same concentration. The sensor shows a low response to methanol, acetone, xylene, benzene and toluene, and almost totally insensitive to CO, H_2, CH_4 and NH_3. The above results indicate that the selectivity of the sensor based on rhombus-shaped Co_3O_4 NR arrays is very high and shows high anti-interference ability. We believe that the high-performance for ethanol detection can be attributed to the unique structure of rhombus-shaped Co_3O_4 NRs with a variety of favorable features, involving good contact, porous structure, high surface-to-volume ratio, high crystallinity and open space.

4 Conclusions

We report a facile fluorine-mediated hydrothermal route to synthesize rhombus-shaped Co_3O_4 nanorod (NR) arrays directly grown on various supporting substrates. The reaction temperature has an obvious impact on the morphology of the precursor. In the growth process, the rhombic Co(OH)F precursor could not be obtained above 100 °C due to the disproportionation of formaldehyde. We also discovered carbonate anions direct the dissolution–recrystallization process. The affinity to Co^{2+} of different anions was found to be in the order of CO_3^{2-} > F^- > OH^-. Co(OH)F can thermally convert to porous Co_3O_4. The NR array-based gas sensor annealed at 450 °C showed the best performance to ethanol detection due to good contact, porous structure, high surface-to-volume ratio, high crystallinity and open space.

Acknowledgements

This work was supported by the National Natural Science Foundation of China 51072181, the Science and Technology Department of Zhejiang Province Project no. 2010R50020.

Notes and references

1 X. Xie, Y. Li, Z. Q. Liu, M. Haruta and W. Shen, *Nature*, 2009, **458**, 746.
2 S. K. Meher and G. R. Rao, *J. Phys. Chem. C*, 2011, **115**, 15646.
3 N. Yan, L. Hu, Y. Li, Y. Wang, H. Zhong, X. Hu, X. Kong and Q. Chen, *J. Phys. Chem. C*, 2012, **116**, 7227.
4 W. Y. Li, L. N. Xu and J. Chen, *Adv. Funct. Mater.*, 2005, **15**, 851.
5 G. Yang, D. Gao, J. Zhang, J. Zhang, Z. Shi, Z. Zhu and D. Xue, *RSC Adv.*, 2013, **3**, 508.
6 Y. Liu, G. Zhu, B. Ge, H. Zhou, A. Yuan and X. Shen, *CrystEngComm*, 2012, **14**, 6264.
7 C. C. Li, X. M. Yin, T. H. Wang and H. C. Zeng, *Chem. Mater.*, 2009, **21**, 4984.
8 X. Xie and W. Shen, *Nanoscale*, 2009, **1**, 50.
9 M. B. Zheng, J. Cao, S.-t. Liao, J. S. Liu, H. Q. Chen, Y. Zhao, W. J. Dai, G. B. Ji, J. M. Cao and J. Tao, *J. Phys. Chem. C*, 2009, **113**, 3887.
10 Y. Li, B. Tan and Y. Wu, *Nano Lett.*, 2007, **8**, 265.
11 X. W. Lou, D. Deng, J. Y. Lee and L. A. Archer, *J. Mater. Chem.*, 2008, **18**, 4397.
12 X. W. Lou, D. Deng, J. Y. Lee, J. Feng and L. A. Archer, *Adv. Mater.*, 2008, **20**, 258.
13 Y. Wang, H. Xia, L. Lu and J. Lin, *ACS Nano*, 2010, **4**, 1425.
14 L. Li, K. H. Seng, Z. Chen, Z. Guo and H. K. Liu, *Nanoscale*, 2013, **5**, 1922.
15 Y. Li, B. Tan and Y. Wu, *J. Am. Chem. Soc.*, 2006, **128**, 14258.
16 X. Xie, P. Shang, Z. Liu, Y. Lv, Y. Li and W. Shen, *J. Phys. Chem. C*, 2010, **114**, 2116.
17 X. Y. Xue, S. Yuan, L. L. Xing, Z. H. Chen, B. He and Y. J. Chen, *Chem. Commun.*, 2011, **47**, 4718.
18 X. H. Xia, J. P. Tu, Y. Q. Zhang, Y. J. Mai, X. L. Wang, C. D. Gu and X. B. Zhao, *RSC Adv.*, 2012, **2**, 1835.
19 H. Nguyen and S. A. El-Safty, *J. Phys. Chem. C*, 2011, **115**, 8466.
20 J. Park, X. Shen and G. Wang, *Sens. Actuators, B*, 2009, **136**, 494.
21 W. Mei, J. Huang, L. Zhu, Z. Ye, Y. Mai and J. Tu, *J. Mater. Chem.*, 2012, **22**, 9315.
22 J. Jiang, J. Zhu, R. Ding, Y. Li, F. Wu, J. Liu and X. Huang, *J. Mater. Chem.*, 2011, **21**, 15969.
23 L. Poul, N. Jouini and F. Fiévet, *Chem. Mater.*, 2000, **12**, 3123–3132.
24 M. Taibi, S. Ammar, N. Jouini and F. Fiévet, *J. Phys. Chem. Solids*, 2006, **67**, 932.
25 Z. Zhao, F. Geng, J. Bai and H. M. Cheng, *J. Phys. Chem. C*, 2007, **111**, 3848.
26 Q. Li, V. Kumar, Y. Li, H. Zhang, T. J. Marks and R. P. H. Chang, *Chem. Mater.*, 2005, **17**, 1001.
27 J. F. Banfield, S. A. Welch, H. Z. Zhang, T. T. Ebert and R. L. Penn, *Science*, 2000, **289**, 751.
28 R. L. Penn and J. F. Banfeld, *Science*, 1998, **281**, 969.
29 C. Pacholski, A. Kornowski and H. Weller, *Angew. Chem., Int. Ed.*, 2002, **41**, 1188.
30 L. Liu, S. Li, J. Zhuang, L. Wang, J. Zhang, H. Li, Z. Liu, Y. Han, X. Jiang and P. Zhang, *Sens. Actuators, B*, 2011, **155**, 782.
31 F. J. Sheini, M. A. More, S. R. Jadkar, K. R. Patil, V. K. Pillai and D. S. Joag, *J. Phys. Chem. C*, 2010, **114**, 3843.
32 H. Yu, D. Wang and M. Y. Han, *J. Am. Chem. Soc.*, 2007, **129**, 2333.
33 C. V. Schenck, J. G. Dillard and J. W. Murray, *J. Colloid Interface Sci.*, 1983, **95**, 398.
34 Q. L. Huang, M. Wang, H. X. Zhong, X.-T. Chen, Z. L. Xue and X. Z. You, *Cryst. Growth Des.*, 2008, **8**, 1412.
35 M. Ghasdi and H. Alamdari, *Sens. Actuators, B*, 2010, **148**, 478.

36 J. Herrán, O. Fernández-González, I. Castro-Hurtado, T. Romero, G. G[a] Mandayo and E. Castaño, *Sens. Actuators, B*, 2010, **149**, 368.
37 K. I. Choi, H. R. Kim, K. M. Kim, D. Liu, G. Cao and J. H. Lee, *Sens. Actuators, B*, 2010, **146**, 183.
38 C. Sun, S. Rajasekhara, Y. Chen and J. B. Goodenough, *Chem. Commun.*, 2011, **47**, 12852.
39 A. M. Cao, J. S. Hu, H. P. Liang, W. G. Song, L. J. Wan, X. L. He, X. G. Gao and S. H. Xia, *J. Phys. Chem. B*, 2006, **110**, 15858.
40 J. W. Yoon, J. K. Choi and J. H. Lee, *Sens. Actuators, B*, 2012, **161**, 570.
41 D. Patil, P. Patil, V. Subramanian, P. A. Joy and H. S. Potdar, *Talanta*, 2010, **81**, 37.